

Chapter 18

Biodegradable Films and Foam of Poly(3-Hydroxybutyrate-*co*-3-hydroxyvalerate) Blended with Silk Fibroin

Amy Tsui,¹ Xiao Hu,² David L. Kaplan,³ and Curtis W. Frank*,¹

¹Department of Chemical Engineering, Stanford University,
Stanford, California 94305-5025

²Department of Physics & Astronomy and Department of Biomedical
Engineering and Sciences, Rowan University, Glassboro, New Jersey 08028

³Department of Biomedical Engineering, Tufts University,
Medford, Massachusetts 02155

*E-mail: curt.frank@stanford.edu

Solvent-cast films of poly(3-hydroxybutyrate-*co*-3-hydroxyvalerate) (PHBV) and silk fibroin (SF) blends were investigated to evaluate miscibility and mutual impacts on thermal properties and morphology to inform how SF may impact the cell microstructure of PHBV foam. It was determined through modulated differential scanning calorimetry (MDSC) and thermal gravimetric analysis (TGA) that the blends were immiscible at all compositions studied. Using attenuated total reflectance Fourier transform infrared spectroscopy (ATR-FTIR), we found that SF morphology changed from amorphous to 38.2-47.6% crystallinity in the presence of PHBV. Additionally, we observed that SF acts as a crystal nucleating agent for PHBV, but subsequently is excluded to the interspherulitic regions during PHBV crystal growth. After melting and fast cooling in the DSC, we found that SF reduces melting temperature and crystallinity of PHBV films, except for 1 and 40 wt% SF, which exhibited anomalous behavior. It is likely that SF nucleates new PHBV crystals, but in regions of higher SF content. The immobile SF causes

more disorder of PHBV crystals near the nuclei resulting in overall lower crystallinity. To produce SF powder for foam extrusion, three 1-day freeze-thaw cycles reproducibly yielded SF aerogels from tough hydrogels after drying in a vacuum oven. These aerogels were ground and added to PHBV and foamed with 0.5, 1, 2, 3, and 4 phr azodicarbonamide (AZ) for 1 wt% SF and 4 phr AZ for 5 wt% SF. Surprisingly, SF actually led to poorer cell density above 0.5 phr AZ, especially for 5 wt% SF due to cell coalescence and greater foam shrinkage during cooling.

Introduction

Over recent decades, there has been a resurgence of effort to develop more sustainable plastics to address environmental and political concerns over the use of fossil fuels and accumulation of alarming levels of plastic in the environment. A particularly attractive option is using a family of biorenewable polyesters called polyhydroxyalkanoates (PHAs). PHAs occur naturally in bacteria, serving as energy storage for times of nutrient limitation. This non-toxic, biodegradable polymer has properties similar to polypropylene (*1*), a ubiquitous plastic found in bottle caps, diapers, containers, and other products. Furthermore, because PHAs are readily found in the environment, anaerobic pathways already exist for their biodegradation. In contrast, poly(lactic acid) (PLA), a synthetic biodegradable polymer that is one of the most commercially prevalent biopolymers, only degrades in industrial composting facilities, not in landfill or marine environments.

Though PHAs are ideal for addressing needs for both renewable feedstocks and biodegradability at end-of-life, they are prone to brittleness and aging effects, and are relatively expensive (*2, 3*). Additionally, their susceptibility to environmental degradation creates drawbacks during processing. They begin to thermally degrade at or above their melting temperature, reducing their already poor melt strength. This is particularly challenging for foam applications where high melt strength and elongational viscosity are important for stabilizing cell growth and achieving uniform, high density cell microstructure and low foam density. Poly(3-hydroxybutyrate-co-3-hydroxyvalerate) (PHBV) is one of the most commonly used PHAs because it has a lower melting temperature than poly(3-hydroxybutyrate) (PHB) and because it is more commercially available than other PHA copolymers. The ability to foam PHA can reduce costs by lowering the amount of polymer required and expand PHA application to packaging (e.g., foam packing), construction (e.g., insulation), and consumer products (e.g., serving ware). Development of PHBV foams for these areas of application has been studied (*4, 5*).

Blending is a common strategy for imparting complementary beneficial properties on polymers in general and on PHAs in particular (*4–7*). Previously, we have shown that blending PHBV with cellulose acetate butyrate, a higher viscosity biodegradable polymer, can result in improved cell uniformity and

lower bulk density at high gas content; however, achievable bulk density was not significantly reduced (4). Cellulose acetate butyrate has been shown to be miscible or partially miscible with PHBV depending on the composition (8). Other blends that have been investigated include PLA/PHBV (7) and PHBV/hyperbranched polymer (5). Miscibility of blend components determines the final properties of the blend since the degree of compatibility will impact the domain size and morphology of the two phases. Because of intermolecular interaction, blend components can also impact the morphology and thermal properties of the other phase, such as by reducing or eliminating crystallinity and melting temperature (8), even in immiscible blends (9). For example, Thirtha et al. (10, 11) documented changes in T_g for immiscible blends, noting that T_g should not change except in cases where there is a difference in thermal expansion coefficients of the components, in which case T_g would increase due to increased pressure at the interface. Reductions in T_g have been observed for non-adhering nanoparticle-filled systems due to the high amount of surface area introduced by the nanoparticles (12). The presence of non-bonded interfaces can increase mobility of chains at the interface and reduce the T_g (10).

A relatively unexplored potential additive for PHBV is silk fibroin (SF), which is the core protein in silk fibers that form silkworm cocoons. Two strands of SF are linked by the glue-like protein sericin, which is further surrounded by a protective protein layer. SF is known for its excellent mechanical properties, including an enhanced elongation-at-break over PHBV (13), and biocompatibility (14, 15), which makes it an attractive candidate for improving the processability of PHBV. The unique mechanical properties originate from the random sequence of amorphous and crystalline regions, which are hydrophilic and hydrophobic, respectively, based on the amino acids that comprise those regions. The crystalline regions form β -sheet structures, also referred to as silk II, through hydrogen-bonding and van der Waals interactions (16, 17). A metastable SF crystalline formation is an α -helix crystal structure, known as silk I (18). Though Sashina et al. (19) determined that SF is immiscible with PHB in films, they also hypothesized that there was some interaction below 20 wt% SF, though they did not probe this composition range. It was also demonstrated that SF could firmly coat a PHA scaffold or film via hydrogen bonding or surface modification (14, 20). Though PHBV has a similar crystal structure as PHB (21), it has been shown that the chains are more flexible and have a lower crystallization ability than PHB (22). It would, therefore, be valuable to investigate the miscibility of PHBV and SF, especially at low concentrations of SF. If SF and PHBV were miscible, SF could potentially enhance the melt strength or subsequent solid mechanical properties. If they are immiscible, the SF phase could serve to nucleate crystal growth, resulting in earlier solidification of foams or to nucleate bubbles to produce higher cell density and more uniform microstructure. Significantly, SF powder has been shown to improve the microstructure of PLA foams with 7 wt% SF by significantly increasing cell density and reducing cell size using a batch foaming process and CO₂ blowing agent (23). Here, we investigate the miscibility of PHBV and SF in films and determine the impact of SF on PHBV foam microstructure to develop a low density, rigid biodegradable foam.

Experimental Materials and Methods

Silk Fibroin Aqueous Solutions

Bombyx mori silk fibroin (SF) aqueous solutions were prepared from silkworm cocoons (Tajima Shoji Co., LTD, Yokohama, Japan), as published previously (24, 25), for film casting and shown in Figure 1. The cocoons were boiled for 30 minutes in 0.02 M sodium carbonate (Alfa Aesar) aqueous solution, then rinsed for 60 minutes in water to remove sericin proteins. The extracted silk was dried overnight, then placed in 9.3 M lithium bromide (Alfa Aesar) aqueous solution for 4–6 hours until all fibers were dissolved, yielding a 20 w/v% solution. This solution was dialyzed in water for three days using Slide-a-Lyzer dialysis cassettes (Pierce, 3500 MWCO) to remove the salt. The SF solution was removed and centrifuged at 13,000 rpm and 10 °C for 40 min until impurities and insoluble SF were pelletized. The final concentration of the aqueous SF solution was ~7 wt% as determined by weighing the solution before and after drying. MilliQ water was used throughout the extraction process.

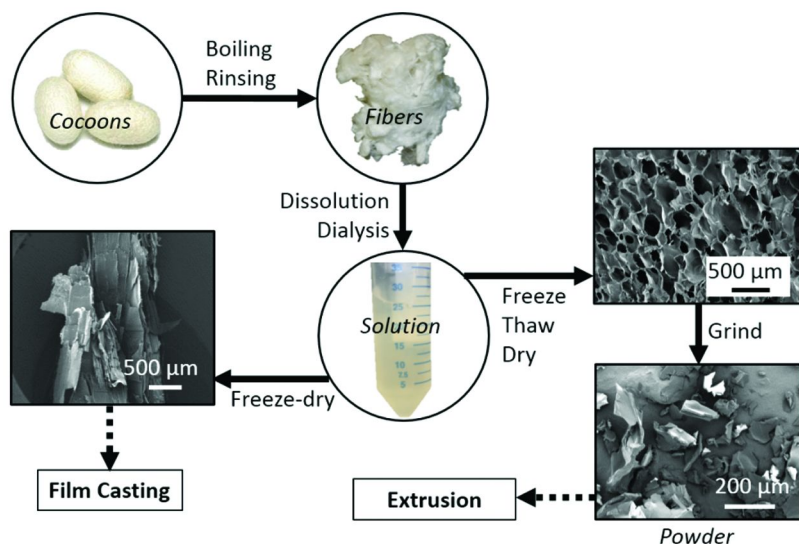


Figure 1. Silk fibroin extraction process to yield material for film casting and extrusion foaming.

Silk Gelation and Powder Preparation

Aqueous SF solutions were frozen at -15 °C, then thawed at 4 °C for a range of freeze-thaw cycles and time periods to form a hydrogel. The minimum total time for a single freeze-thaw cycle to form a gel was determined systematically using 1 mL aqueous SF solutions. When solutions had gelled, the color was white and there was no flow upon inversion. Multiple freeze-thaw cycles were applied to 10 mL samples to reduce overall time for gel formation and improve the toughness of the gels. 10 vol% methanol was also added to some SF solutions

to induce gelation earlier; these gels were translucent after gelation. However, the resulting gels were easily broken and yielded an extremely friable and yellowed dried structure. Therefore, methanol was not effective in forming SF powder in this process, so is not discussed further. After cycles where gel formation was observed, small samples were removed for drying to determine when the bulk could dry into grindable material. The tough gels were dried in a vacuum oven at 70 °C for at least 24 hours. Dried gels that formed a low density solid were ground with mortar and pestle or a coffee bean grinder for a few seconds to a powder of heterogeneous diameter and shape, as shown in Figure 1. Large particles were removed using a sieve with 1 mm mesh size before extrusion.

PHBV/SF Film Preparation

Poly(3-hydroxybutyrate-co-3-hydroxyvalerate) (PHBV) with 5 mol% hydroxyvalerate content (trade name ENMAT Y1000) was obtained from Tianan Biologic Materials Company, Ningbo, China and appears as a white powder. The batch of PHBV used for films has a weight-average molecular weight (M_w) of 374k and polydispersity of 4.58, as determined from gel permeation chromatography (GPC). SF aqueous solutions were dried by first freezing the solution at -80 °C overnight, then lyophilizing in a Labconco FreeZone6L Freeze Dry System for 2-3 days until completely dried to achieve a relatively soft, solid material from which small flakes could be manually torn.

Hexafluoroisopropanol (HFIP, Sigma-Aldrich) was used as a common solvent for PHBV and SF. PHBV and SF were refluxed in HFIP for 24 hours at the following PHBV/SF compositions: 100/0 (PHBV), 99/1 (P99S1), 95/5 (P95S5), 90/10 (P90S10), 80/20 (P80S20), 60/40 (P60S40), 40/60 (P40S60) and 0/100 (SF). 90/10 PHBV/SF (P90S10) blend film was produced for observation of film morphology using SEM and for thermal transitions in DSC. The blended solution was poured into a shallow glass petri dish and covered loosely with aluminum foil for solvent casting. HFIP was allowed to evaporate from the solution for 24 hours in a fume hood, then further dried for 3 days in a vacuum desiccator to ensure complete removal of solvent.

Thermal Analysis of Films

Thermal transitions of PHBV/SF blended films were measured with a TA Instruments Q100 differential scanning calorimeter (DSC) at a nitrogen flow rate of 50 mL/min with temperature modulation. Small samples were encapsulated in aluminum pans and heated from -40 °C to 200 °C in the first heating cycle and from -45 °C to 300 °C in the second heating cycle with modulation of 0.32 °C every 60 seconds and at a rate of 2 °C/min throughout. Between heating cycles, samples were cooled quickly to -45 °C to retain maximum levels of amorphous regions in the films, thus accentuating T_g , which was taken to be the midpoint of the heat capacity change during this second heating cycle on the reversing heat flow curve. Other thermal transitions were taken from the total heat flow second heating cycle. The melting temperature, T_m , was measured from the endothermic peak and the crystallization temperature was taken as the peak temperature of the

exothermic peak. Decomposition endotherms of PHBV and SF were observed as separate peaks above 200 °C. However, the decomposition temperatures from DSC are not discussed due to potential mass loss causing possibility for error.

Instead, a TA Instruments Q500 thermal gravimetric analyzer (TGA) was used to accurately determine decomposition temperature. Small samples were heated from room temperature to 500 °C at 5 °C/min under a nitrogen atmosphere. The decomposition temperature at the maximum rate of degradation, $T_{d\max}$, was taken as the peak of the differential TGA (DTGA) weight loss curves.

Film Morphology Characterization

Attenuated total reflectance Fourier transform infrared (ATR-FTIR) spectra of PHBV/SF blend films and SF materials were obtained using a Jasco 6200 FTIR spectrometer with ATR crystal accessory at 4 cm⁻¹ resolution. The spectra for the blends were normalized to the 1340-1400 cm⁻¹ region. The peaks were fitted using the multi-fit tool in the Origin 8 software (OriginLab, USA) applying a Lorentzian fitting. The number of peaks was determined in advance of fitting based on the observed and expected peaks in the spectrum.

Film morphology was observed with a scanning electron microscope (SEM, FEI XL30 Sirion with FEG source) after sputter-coating with Au60Pd40 alloy using a Gressington 108Auto sputter coater operated at 20 mA for 30 seconds. The average distance between spherulites, D_s , was measured using ImageJ image analysis software (available through the National Institutes of Health).

PHBV/SF Foam Processing

The pelletized form of PHBV with 5 mol% hydroxyvalerate content (trade name ENMAT Y1000P) (Tianan Biologic Materials Company, Ningbo, China) was blended with the powdered PHBV (ENMAT Y1000) for foam processing. ENMAT Y1000P had a M_w of 394K and polydispersity of 2.80, as determined from GPC. The batch of ENMAT Y1000 used for extrusion foaming had a M_w of 701K and polydispersity of 4.19, as determined from GPC. Powder and pellet PHBV were blended at a composition of 10/90 by weight in order to retain as much blowing agent as possible during material transfer to the extruder hopper.

The chemical blowing agent utilized in this study is activated azodicarbonamide (AZ) (trade name Actafoam 765A) from Chemtura. This blowing agent is a fine yellow powder that decomposes in the temperature range of 152 to 160 °C, generating approximately 180 cc of gas per gram of solid, most of which is nitrogen, according to the manufacturer.

PHBV was dried at 100 °C for at least 90 minutes before dry blending with 1 wt% SF powder and AZ. AZ content was 0, 0.5, 1, 2, 3, and 4 parts per hundred grams of polymer (phr). The dry blends were extruded through a 3/4 inch single-screw extruder (L/D ratio 25:1, compression ratio 3:1, C.W. Brabender) equipped with a 2-inch horizontal flex-lip ribbon die fixed at 1 mm thickness. The screw rotation speed was 80 rpm. The extruder temperature profile was set at 150 °C, 170 °C, 160 °C, and 150 °C, from the hopper to the die. The extruder was cleaned using Sample X purging compound kindly supplied by DynaPurge, NY.

Foam Characterization

Samples from foam produced after approximately four minutes of extrusion at a given composition were cryo-fractured to expose the cellular morphology along the direction of extrusion at the center point of the foam width. Samples were sputter-coated as described earlier for films, but for 90 seconds to completely coat the porous structure, then imaged using SEM. The outlines of each cell were manually drawn using a Bamboo Capture tablet (Wacom, USA) so that ImageJ software (NIH) could be used to analyze the cells to provide number of cells (N), sampling area (A), and cell area. For each foam composition, cells were counted within a sampling area of around 7 cm^2 .

The cell density, n_b , was calculated as follows:

$$n_b = \left(\frac{N}{A}\right)^{3/2} m E$$

where m is the unit conversion to achieve cubic centimeter units. The exponent is for the conversion from an area to volume basis. The expansion ratio, E , is determined by:

$$E = \frac{\rho_u}{\rho_f}$$

Bulk density of foam samples, ρ_f , and unfoamed samples, ρ_u , is measured using the water displacement method.

Characterization of PHBV/SF Blend Films

Results

Glass Transition of PHBV/SF Blend Films

The total heat flow DSC thermograms from the second heating cycle are shown in Figure 2(a) and the thermal transitions observed in the second heating curves are summarized in Table I. In this study, a fast cooling cycle was utilized to kinetically trap the polymer chains in a more amorphous stage. As such, the T_g is only observable in the second DSC heating cycle after this fast cooling cycle and the reversing heat flow thermograms highlighting the PHBV T_g range are shown in Figure 2(b). T_g s of the PHBV/SF films were observed between -4.2 — 1.1 °C. T_g of SF was not observable in SF films along the entire thermogram, although it has been measured previously in references (26, 27).

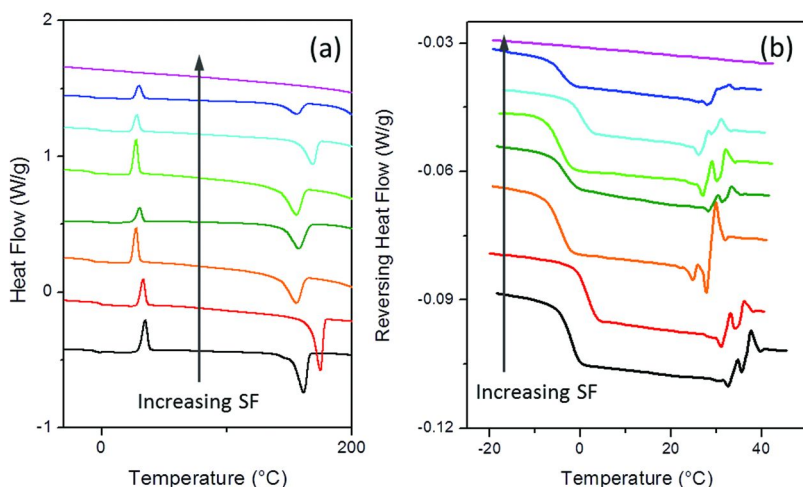


Figure 2. DSC thermograms from the second heating cycle of PHBV films with SF content ranging from 0 to 100 wt% showing the (a) total heat flow curve for the entire temperature range and (b) reversing heat flow curve of temperature range of the PHBV glass transition. From bottom: PHBV, P99S1, P95S5, P90S10, P80S20, P60S40, P40S60, and SF.

Complete miscibility of two polymers is typically expressed through the presence of a single thermal transition that is intermediate to those of the neat polymers. For example, T_g of a miscible blend may follow the Fox-Flory equation, which is given by:

$$\frac{1}{T_g} = \frac{w_1}{T_{g1}} + \frac{w_2}{T_{g2}}$$

where w_i and T_{gi} are the weight fraction and T_g , respectively, of each phase, i . In the case of the compositions studied here, T_g of a miscible SF-PHBV blend would be expected to range from -1.1 °C for P99S1 to 82.1 °C for P40S60. Clearly, the blend T_g s do not follow these predicted T_g values, which indicates that SF and PHBV are immiscible at the compositions studied. Most of the blend compositions exhibit a lower T_g , which generally reflects a greater amount of free volume or disorder in the system such that the material requires less thermal energy to achieve the glass transition. For P99S1 and P60S40, the T_g is slightly greater than that of PHBV, particularly P99S1, whose T_g surpasses what would be predicted by Fox-Flory. The overall change is small, however, and may simply be within experimental error.

Table I. Thermal properties of PHBV/SF blends from the 2nd DSC heating cycle

<i>Sample</i>	<i>T_g</i> (°C)	<i>T_m</i> (°C)	<i>T_c</i> (°C)	<i>ΔH_m</i> (J/g)	<i>χ_c</i> (%)
PHBV	-2.2	161.3	30.2	84.4	57.8
P99S1	1.1	174.8	33.2	85.3	59.0
P95S5	-4.2	155.5	27.5	77.9	52.8
P90S10	-3.7	157.3	30.4	71.0	54.0
P80S20	-4.1	154.9	29.2	64.3	55.1
P60S40	0.1	168.6	28.1	50.7	57.9
P40S60	-4.1	155.9	29.9	29.8	51.0
SF	175-180 ^a	NE ^b	NE	NE	NE

^a Reference (26, 27). ^b NE – Nonexistent.

Melting and Crystallization Properties of PHBV/SF Blend Films

In films containing PHBV, endotherms were present in the range of 130-185 °C corresponding to melting peaks of PHBV, as shown in Figure 2(a) and summarized in Table I. In general, melting temperature decreases with increasing SF content. Again, P99S1 and P60S40 samples appear anomalous.

From the melting endotherm, a relative degree of crystallinity, x_c , can also be calculated. The degree of crystallinity of the PHBV phase was determined by

$$x_c = \frac{(\Delta H_m)/n}{\Delta H_m^\circ} \times 100\%$$

where ΔH_m is the heat of enthalpy of melting and n is the weight fraction of PHBV. ΔH_m° is the heat of melting of 100% crystalline PHB and was taken to be 146 J/g (28). We do not subtract the heat of enthalpy of crystallization, and thus the crystallization upon heating is included in the final crystallinity. From this calculation, as shown in Table I, it is observed that the degree of crystallinity generally decreases with SF content in the second heating cycle.

The presence of a crystallization peak between 27.5 and 33.2 °C in the second heating cycle, as shown in Figure 2(a), is expected to be due to crystallization of amorphous PHBV after devitrification. The crystallization peak coincides with fluctuations and then increase in the baseline heat flow observed in Figure 2(b). Though reorganization is typically expressed in the non-reversing heat flow (29), the increase in the heat flow baseline suggests a more ordered structure. Additionally, the crystallization peak only appears in the second heating cycle, so it must be associated with the presence of a higher amorphous content after fast cooling.

Thermal Degradation of SF/PHBV Blend Films

The degradation temperatures were determined using TGA and DTGA, as shown in Figures 3(a) and 3(b), respectively, and summarized in Table II. The SF phase was too small to exhibit a decomposition curve for P99S1. The heating curves in Figures 3(a) and 3(b) both exhibit two distinct degradation behaviors corresponding to PHBV, then SF degradation. These two phases of degradation support the conclusion that PHBV and SF are immiscible. However, the PHBV and SF phases do affect the thermal properties of the other phase, suggesting that there is some degree of interaction.

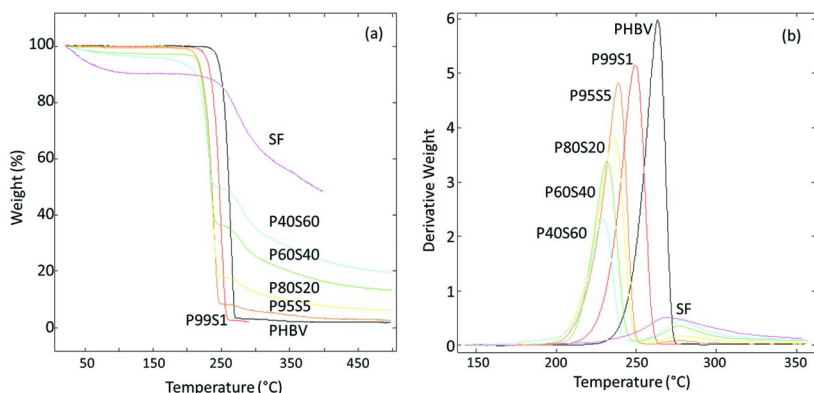


Figure 3. (a) TGA weight loss curves of SF and PHBV blends, and (b) DTGA weight loss curves of SF and PHBV blends.

Table II. Degradation temperatures determined from TGA

Sample	PHBV $T_{d \text{ max DTGA}}$ (°C)	SF $T_{d \text{ max DTGA}}$ (°C)
PHBV	263.38	--
P99S1	249.33	N.D. ^a
P95S5	238.72	277.55
P80S20	235.91	278.69
P60S40	231.59	276.96
P40S60	229.36	277.98
SF	--	268.48

^a N.D. – not determined.

The initial plateau present in Figure 3(a) at higher silk contents is associated with loss of bound water (19), and shows a proportional increase in water content with SF content. It is also apparent from the DTGA curves in Figure 3(b) that the temperature at maximum degradation rate, $T_{d \max}$, of the PHBV phase decreases monotonically with increasing SF content. Because PHBV is susceptible to hydrolysis (30), especially at elevated temperatures, the reduction in T_d of PHBV is likely due to the presence of bound water associated with the SF. Additionally, PHBV chain ends at the interface of the two polymer phases would be more mobile, which could allow for easier chain backbiting to form the six-membered ring intermediate in the PHBV thermal degradation mechanism (31). This could be potentially detrimental to the PHBV processability. In contrast, $T_{d \max}$ of the silk phase increases almost 10 °C with presence of PHBV.

Morphology of SF/PHBV Blend Films

Figure 4 shows the SEM images of the different film compositions. With up to 10% SF, the interspherulitic boundaries remain distinct and even show some detachment between spherulites, which could result in brittleness. With increased SF content, the interspherulitic boundaries become less distinct and no detachment is observed. In the PHBV phases, the average distances between the PHBV nuclei, D_s , can be measured and are listed in Table III. With inclusion of silk, D_s more than doubles suggesting that there are fewer crystal nucleating sites, so crystals can grow much larger before impingement. Additionally, the standard deviation, σ , of D_s increases as well, reflecting a higher distribution of spherulite sizes. It is possible that SF is nonuniformly distributed in the film or that homogeneous nucleation occurs as well after additional cooling.

ATR-FTIR can provide more insights into the morphological changes occurring in both phases. FTIR has been applied widely to quantitatively study polymer crystallinity and crystallization (32–34). In SF, the absorbance spectrum is divided into the amide I (1700–1600 cm^{-1}), amide II (1600–1500 cm^{-1}), and amide III (1350–1200 cm^{-1}) regions (35). The amide I region is most often used to quantitatively evaluate secondary SF structure (35, 36). Within this region, the C=O stretching vibration will shift from around 1646 to 1624 cm^{-1} corresponding to the amorphous and crystalline regions, respectively, with the formation of β -sheet crystals (35, 37). The amide II region is mostly associated with C–N stretching and N–H in-plane bending vibrations where there is a shift from 1537–1545 to 1526 cm^{-1} corresponding to crystalline or amorphous phases, respectively (35, 37). The region of C=O stretching vibration for amorphous and crystalline PHBV is around 1740 and 1720 cm^{-1} , respectively (32, 33, 38). Figure 5 shows the absorption spectra from 1800 to 1550 cm^{-1} of the blend compositions.

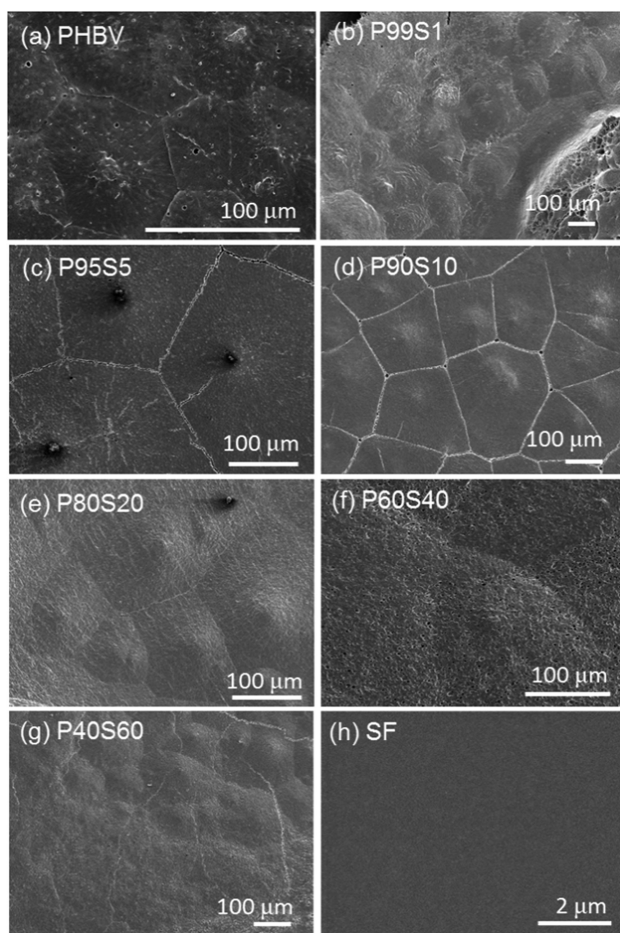


Figure 4. SEM images showing spherulitic formation in (a) PHBV, (b) P99S1, (c) P95S5, (d) P90S10, (e) P80S20, (f) P60S40, (g) P40S60, and (h) SF films.

Table III. Average distance between PHBV nuclei

<i>Sample</i>	<i>D_s (μm)</i>	<i>σ (μm)</i>
PHBV	60.9	13.9
P99S1	179.4	49.2
P95S5	252.6	80.2
P90S10	174.7	62.3
P80S20	156.4	64.2
P60S40	256.1	74.8
P40S60	130.7	38.7

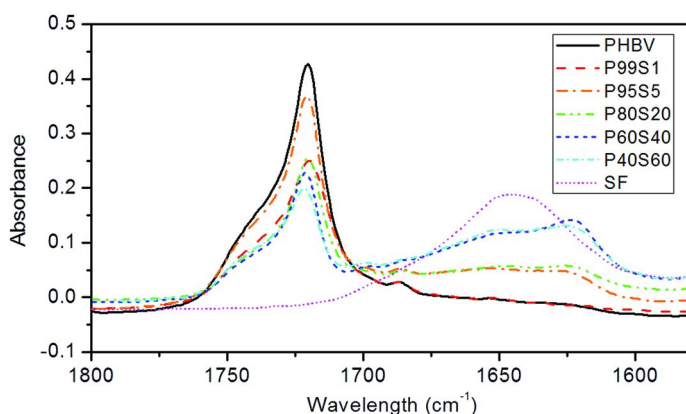


Figure 5. FTIR absorbance spectra of PHBV/SF blends from 1580-1800 cm⁻¹.

There is a clear shift in the SF carbonyl-stretching region (1700-1600 cm⁻¹) from amorphous to increasing crystalline structure in SF. Any shift in the PHBV carbonyl-stretching region (1750-1700 cm⁻¹) is less obvious, but the crystallinity of SF and PHBV can be calculated from the FTIR data using the following equations:

$$\text{PHBV: } x = \frac{A_{1724}}{A_{1724} + A_{1740}} \times 100\%$$

$$\text{SF: } x = \frac{A_{1624}}{A_{1624} + A_{1646}} \times 100\%$$

where $A_{\text{wavenumber}}$ is the absorbance peak intensity, which is determined using a multi-peak fitting. To produce the best fitting, a broader region of wavenumbers was selected, from 1400-1800 cm⁻¹. This included the peak at 1515 cm⁻¹ associated with vibrations in tyrosine in SF (35) and C=O and O-H interaction in PHBV crystals (1686-1690 cm⁻¹) (33) and CH₂ scissoring in PHBV (1453 cm⁻¹) (32). Representative peak fittings are shown in Figures 6(a)-(c), and all had R-squared values above 99.6%.

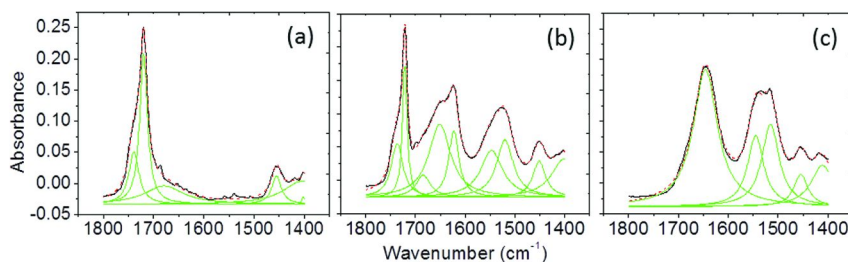


Figure 6. Representative FTIR absorbance spectra with deconvoluted peaks for (a) PHBV, (b) P60S40, and (c) SF. Black line is original data, dashed line is total fit, and lighter peaks are the deconvoluted peaks.

Figure 7 compares the crystallinities calculated from DSC and FTIR for PHBV and SF. SF appears to remain amorphous from 0-1 wt% SF, but it is likely that the crystalline portion in SF is difficult to detect in FTIR for P99S1. At 5 wt% SF, there is a marked jump to 38% crystallinity. PHBV crystallinity calculated from FTIR is higher than that calculated from the second heat cycle of DSC by 15.5 percentage points on average.

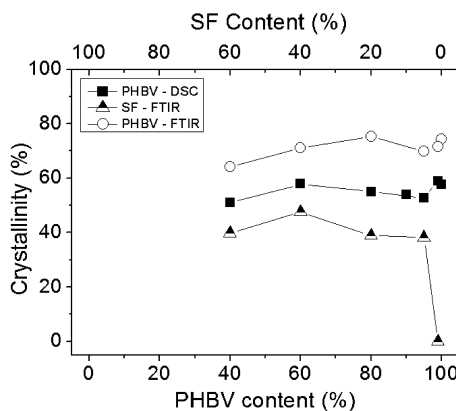


Figure 7. Crystallinity of PHBV and SF versus blend composition from DSC and FTIR.

The difference in crystallinity values determined by FTIR and DSC is primarily due to the pre-measurement processing. The crystallinity from DSC was taken after a fast cooling cycle that hinders crystallization. Thermal degradation of PHBV during slow heating in MDSC may also contribute to lower crystallinity as well as the fact that crystallinity from DSC is calculated with respect to a purely crystalline PHB rather than PHBV. From both FTIR and DSC, crystallinity appears to decrease at P95S5 by about 5% before returning to the maximum at P80S20 for FTIR or P60S40 for DSC. P40S60 has the lowest PHBV crystallinity in both cases.

Discussion

Structure and Property Development of PHBV/SF Due to Film Casting

In the case of neat PHBV, crystallization of the film can proceed without hindrance as solvent evaporates. As such, the film produced is highly crystalline (74.4% by FTIR) with more uniformly dispersed spherulites. Assuming no impurities, nucleation of the crystals is a homogeneous process where the nuclei are formed spontaneously when enough energy is introduced to the system, e.g., through solvent evaporation and cooling, as diagrammed in Figure 8(a).

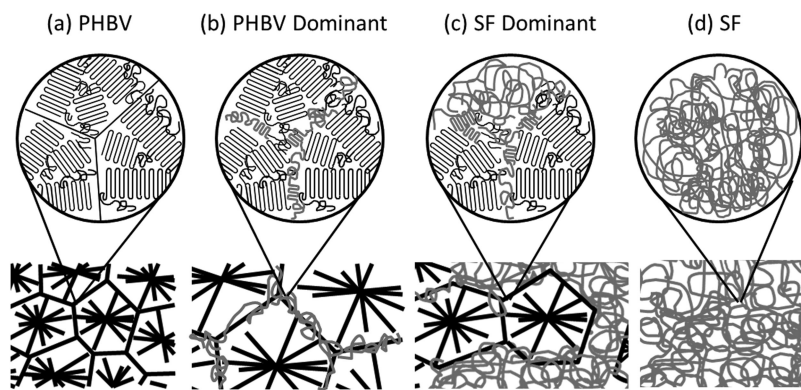


Figure 8. Proposed morphology of PHBV/SF films, where PHBV is black and SF is gray. (a) 100% PHBV is highly crystalline with distinct spherulites formed from homogeneous nucleation. (b) Up to 40 wt% SF, SF acts as a nucleating agent for PHBV and is also excluded to the interspherulitic regions where SF may form β -sheet crystals. (c) At 60% SF, SF continues to reduce PHBV crystallinity while the PHBV nucleates SF β -sheet crystals. (d) SF films are completely amorphous.

For SF and PHBV dissolved in solution, the two phases are initially mixed due to a common solvent. As the solvent evaporates, the SF must associate with itself or with PHBV. At the interfaces between SF and PHBV, there may be some interaction between hydrophobic PHBV and the hydrophobic regions of SF. This may promote some agglomeration and then crystallization of the SF hydrophobic regions, expressed in Figures 8(b)–8(c). During degradation, β -sheet crystals are known to be very resistant to thermal decomposition, and more resistant than amorphous SF (36, 37, 39, 40). The shift of SF to becoming a semi-crystalline material, as shown using FTIR, is thus consistent with the shift of SF to higher degradation temperatures observed using TGA. As the SF crystallizes, it may also then simultaneously serve as a heterogeneous nucleating agent for PHBV crystals. Heterogeneous nucleation requires less activation energy to generate crystal nuclei so can occur earlier. Since SF is not miscible in PHBV, the dispersion is poor so there are fewer nucleation sites that are not uniformly distributed. This is reflected in the increased D_s and large standard deviation of spherulite size observed in SEM.

Over time, the two phases will phase separate in solution since they were shown earlier to be immiscible without solvent. The competition between crystallization and phase separation for a blend of semicrystalline and amorphous polymers was investigated by Tanaka and Nishi (41) who found that the amorphous polymer acts as an impurity and is excluded to the interlamellar regions. Di Lorenzo (42) stated that not all particles will be pushed to the boundaries; this will depend on the balance of energy required for incorporating, removing, and deforming the particle. Therefore, as the crystallization of PHBV proceeds and solvent continues to evaporate during film casting, some SF may become trapped in the interlamellar regions of a growing spherulite while other SF may be excluded and segregated to the interspherulitic regions. Considering that the interspherulitic boundaries observed in SEM become less distinct with increasing SF content, it is likely that SF is becoming constrained to these regions and the constraint as well as hydrophobic surroundings may induce a restructuring of the chain to form β -sheet crystals, which will occupy less volume and are hydrophobic. This proposed change in morphology is expressed in Figure 8(b). Additionally, since crystallization was allowed to occur over several days, the presence of residual solvent during this time could lead to improved crystalline morphology. Genovese and Shanks (43) observed a similar phenomenon when blending immiscible isotactic polypropylene and poly(ethylene-co-methyl acrylate) (EMA), both semicrystalline polymers. They found that EMA reduced the nucleation density of PP spherulites, though did not decrease the crystallization rate and crystallinity. They also proposed that the EMA was pushed to the interspherulitic regions.

In the unique case where SF is less than 20 wt% SF, the degree of crystallinity of PHBV showed a local minimum at 5 wt% SF according to FTIR. In this range, it appears that there is increased interaction between PHBV and SF. For example, 1 wt% SF achieves the same decrease in crystallinity of the PHBV phase as 40 wt% SF. If the 1 wt% SF is more dispersed in the PHBV phase due to higher interaction, more interfaces are present that generate greater mobility of adjacent PHBV chains. This would also explain the much larger rate of degradation decrease of PHBV T_d of P99S1 and P95S5. At larger SF concentrations, there may be a greater driving force for phase separation to reduce interfacial regions.

Where SF is the major phase, as shown in Figure 8(c), the crystalline regions of PHBV may serve as heterogeneous nucleation sites for crystal formation or phase separation may have also contributed to β -sheet formation. In this case, the PHBV phase was slightly less crystalline. PHBV may be more disperse and not able to crystallize to completion. Films of SF remain amorphous, as depicted in Figure 8(d).

Structure and Property Development of PHBV/SF Due to Fast Cooling From Melt

After the fast cooling cycle in DSC, there was an overall reduction in crystallinity and some reduction of T_g of the SF/PHBV blends with 5 wt% SF or greater compared to PHBV. Sashina et al. (19) proposed that SF had a plasticizing effect for compositions with less than 20 wt% SF content. Another explanation is

that because the SF phase does not melt during the first heating cycle it remains a solid during subsequent cooling and heating steps. The presence of this solid particle can act as a nucleating agent for PHBV crystallization, as diagrammed in Figure 9. The new site of the PHBV crystal nuclei would be located near regions of higher SF content and may already be entangled in the SF phase so crystallization will be hindered in these vicinities. Therefore, the presence of SF as a nucleating agent and source of crystal imperfections is important in the increased amorphous fraction in PHBV/SF blended films after quenching in the DSC.

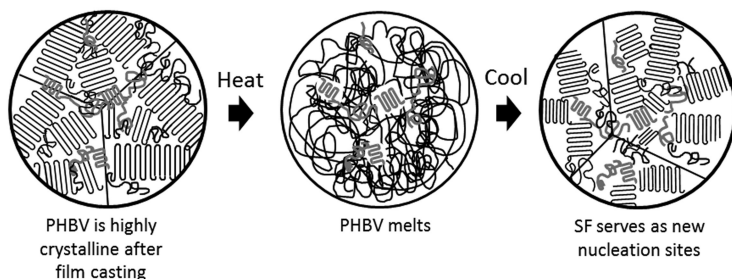


Figure 9. Structure development of PHBV morphology from PHBV/SF blends in the DSC. The PHBV phase is highly crystalline after film casting with SF primarily constrained to interlamellar regions. Upon heating, the PHBV melts while the SF remains a solid. On fast quenching, SF acts as a nucleating agent for new PHBV spherulites. However, the local area is more highly concentrated with SF which leads to more disordered and less crystal formation.

Because the structure is forming from the melt stage, the properties here more reflect phenomena that could occur during extrusion. For extrusion foaming, higher crystallinity is more important for stabilizing the foams in a solid structure, preferably before cell coalescence can happen. To take advantage of the nucleating behavior of SF while minimizing additional thermal degradation, SF powder was blended with PHBV at low concentrations for foam extrusion.

Development of Silk Gelation Process for Powder Production

Results

Silk fibroin powder is not readily available through chemical manufacturers in the US, although it is used commercially in a degraded form by the cosmetics industry (44). The freeze-dried SF produced for use in films is not able to be ground into powder. Water evacuation from SF during lyophilization and lack of a tough physical gel network causes a collapsed layered sheet structure, as shown in Figure 10. Instead, a silk aerogel must be made. An aerogel is a dry gel with high porosity where the liquid has been replaced by a gas without collapsing the wet gel structure (45). Kim et al. (24) prepared silk hydrogels at room temperature and higher, and the resulting freeze-dried structure was highly porous. While silk hydrogels have been studied extensively, it has been in the context of biomaterials for cell scaffolds (25) and drug delivery (24, 46).

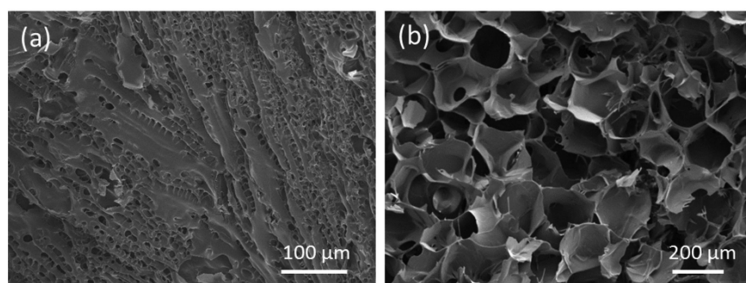


Figure 10. Microstructure of dried SF when (a) freeze-dried from aqueous solution and (b) dried in an oven after freeze-thawing to form a gel.

We have developed a simple process that can lead to a brittle porous material for grinding into powder. This process is outlined in Figure 1 and involves freezing the aqueous SF solution at $-15\text{ }^{\circ}\text{C}$ to form a solid, then thawing at $4\text{ }^{\circ}\text{C}$. Over time, gelation will occur and the resulting gel is vacuum-dried at $70\text{ }^{\circ}\text{C}$ to reveal a brittle, dry solid that can be ground with a mortar and pestle to powder, as shown in Figure 1. As expected, the processing procedure of the SF solutions has a significant impact on the final bulk morphology, as shown in Figure 10(a)-(b). In the freeze-drying process used in this work, any pores left by water collapse to form sheets (Figure 10(a)), while the pores will remain open when freeze-thawed to form a gel and then dried in a vacuum oven at $70\text{ }^{\circ}\text{C}$ (Figure 10(b)).

Single Freeze–Thaw Cycle for SF Gelation

A time study to determine the minimum overall time required to produce a silk hydrogel was carried out using 1 mL samples, and the results are shown in Figure 11(a). These gels were not dried following gelation. With increasing days at $-15\text{ }^{\circ}\text{C}$, the time to gelation at $4\text{ }^{\circ}\text{C}$ decreased. After 12 days in the freezer, gelation would reach completion in the $-15\text{ }^{\circ}\text{C}$ environment such that it would already be a gel upon thawing. It appeared that the minimum time required was 6 days of freezing at $-15\text{ }^{\circ}\text{C}$ and 2 days of thawing at $4\text{ }^{\circ}\text{C}$ or 8 days total. Faster gelation upon thawing occurred for all samples with greater than 6 days of freezing. When using room temperature for the thawing stage, the time to gelation was generally longer, as shown in Figure 11(b). The shortest time to achieve a gel was 19 days or 14 days of freezing and 5 days of thawing. Therefore, subsequent SF gelation experiments were performed using at $4\text{ }^{\circ}\text{C}$ thawing temperature.

Multiple Freeze–Thaw Cycling for SF Gelation

The effect of freeze-thaw cycling on SF was investigated to determine whether the gelation process could be improved in terms of reproducibility and length of time; the various freeze-thaw cycling schemes are summarized in Table IV. In this study, 10 mL samples were used to reduce any surface effects from the container

and evaluate a bulk state; each scheme used 4 samples. The results of the total cycles and days required to produce a tough hydrogel that could be potentially ground are shown in Figure 12. Scheme 24 resulted in grindable foams for all four samples after 4 cycles or 8 days. This scheme was chosen to produce more aerogels using 30 mL samples. The result was 8 of 9 large samples yielding grindable foams with an average of 3.1 ± 1.1 cycles and 7.9 ± 3.2 days. Some of the foams showed some shrinkage after drying, with very large pores, but could still be ground. The schemes with longer cycles required many more days before gelation and resulted in solids that were yellowed and collapsed so were unable to be ground. Scheme 72 yielded gels that were very difficult to dry for the conditions used; after many days of drying, the gels remained mostly hydrated. In all cases, at least three cycles were required before gel formation occurred. Foams that could be ground had large pores after drying, as shown in Figure 10(b).

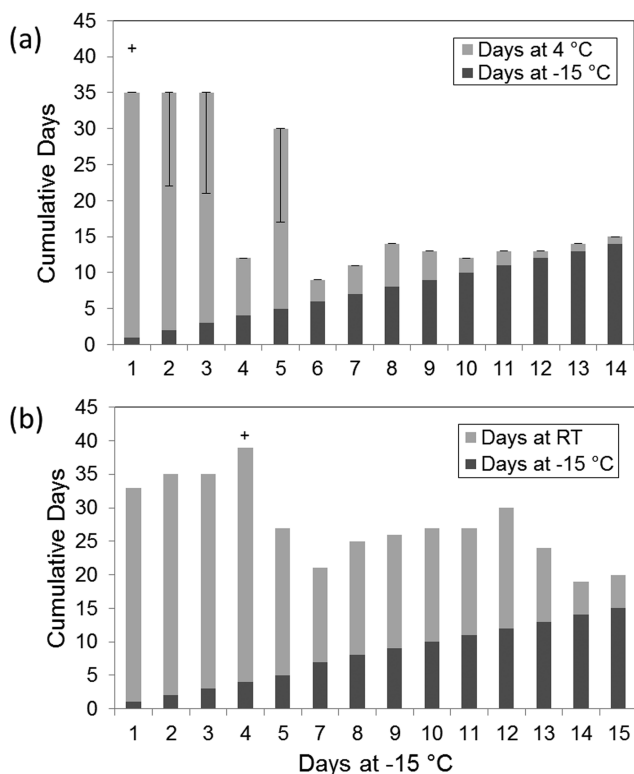


Figure 11. The total number of days to achieve a gel through one cycle of freezing the SF aqueous solution at -15 °C for 1-14 days then thawing at (a) 4 °C and (b) room temperature (RT) until a gel is formed. + indicates that the sample did not achieve gelation within the experimental time frame.

Table IV. Freeze–thaw cycling schemes for achieving silk gelation

<i>Scheme Abbreviation</i>	<i>Freeze Time at -15 °C (days)</i>	<i>Thaw Time at 4 °C (days)</i>
Q	Shortest time to freeze (average 0.45 ± 0.22)	Shortest time to thaw (average 0.59 ± 0.20)
12	0.5	1
24	1	1
48	2	2
72	3	3
321	Cycle 1: 3 days Cycle 2: 2 days Cycle 3+: 1 day	Cycle 1: 3 days Cycle 2: 2 days Cycle 3+: 1 day

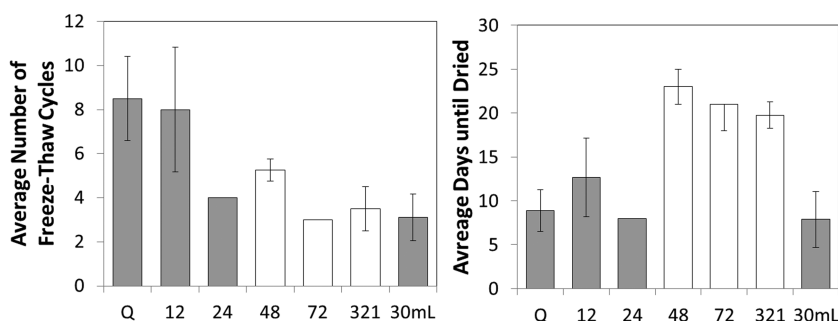


Figure 12. Results of freeze-thaw cycling. (a) Average number of freeze-thaw cycles and (b) average number of days until gel could be dried. Gray bars yielded foams that could be ground into powder while white bars did not. Error bars are the standard deviation of four samples except for Scheme 72 in (b) which reflects drying that could have occurred earlier.

Discussion: Impact of Temperature, Time, and Cycling on Gelation of SF

If the aqueous SF solution does not undergo freezing, storage of the solution at higher temperatures will lead to faster gelation compared to storage at low temperature. Jin and Kaplan (47) found that storing an 8% SF solution at room temperature will lead to hydrogelation in about 5 days compared to about 40 days at 7 °C. It has been shown that silk gelation at room temperature and physiological temperature occurs over two stages. The first stage is association of chains through weaker interchain interactions such as hydrogen bonding, hydrophobic interactions, and electrostatic interactions. After more time, β -sheets form and these physical crosslinks are to be considered irreversible (48). However, gels formed without a freeze step likely have poor mechanical properties not conducive to maintaining a porous structure during drying. We found that gels

formed at 4 °C for more than one year had very poor tear strength and would dry to a yellowed, non-porous solid. Similarly, poly(vinyl alcohol) (PVA) will gel over time at room temperature, but the resulting toughness is poor (49). In fact, highly elastic PVA gels can only be formed after repeated freeze-thaw cycles (49).

Once the SF solution has been frozen, we observed that gelation occurred more quickly when thawing SF at 4 °C rather than room temperature. It has been hypothesized that the freezing of the water molecules in a PVA solution leads to exclusion of PVA from the ice crystals and then gel formation (50). A similar mechanism may be occurring in SF solution. In aqueous solution, the water interacts with the hydrophilic regions of the SF chain, which stabilizes the amorphous conformation and prevents crystallization in solution (47). Exclusion of the polymer from the water will promote interchain interactions and formation of β -sheet crystals and thus reduce the time required to form a tough, irreversible network. As the hydrophobic β -sheet crystals form, water will also be excluded from the SF phase forming a larger water phase. By thawing at cooler temperatures, the melting of ice is delayed, which could allow more time for the silk to form β -sheets from the amorphous regions before they may reassociate with water molecules.

Nazarov et al. (25) found that freezing of aqueous SF solution at particular temperatures would impact the pore size of the resulting dried gel. If the freezing temperature was within the T_g of aqueous silk (-20 to -34 °C (51)), pore sizes from ice crystallization were large. Freezing below this range resulted in small pores due to fast ice crystallization. Peppas and Stauffer (50) attributed larger pore size of PVA gels to the continued perfection of ice crystals. This perfection was also promoted through repeated PVA freeze-thaw cycling, which could explain why all freeze-thaw cycling schemes investigated in this work required at least 3 cycles on average before forming an appropriate gel for grinding. The fastest gel formation scheme when performing multiple freeze-thaw cycling required 4 total days of freezing as opposed to a single freeze-thaw cycle which required 6 continuous days of freezing, though both methods led to gels in 8 total days.

Furthermore, Li et al. (51) reported that the freezing temperature affected the SF chain morphology. Freezing above -20 °C led to SF that was composed significantly of α -helices, while below -20 °C would lead to primarily amorphous SF and some β -sheets. These foams were immediately freeze-dried and the resulting foams were described as “spongy,” which may imply that they would be too soft for grinding. In the present study, freezing of SF was performed at -15 °C, yet the resulting gel and dried foam did have β -sheet formation according to FTIR. Because α -helices are metastable, the thawing period may have provided sufficient time for the change to β -sheets. These considerations also suggest that the lyophilization process used in this study may not have been conducive to porous foam formation. The short freezing time at -80 °C followed by immediate freeze-drying did not allow time for SF to self-associate enough to form a tough gel structure to support the porous structure when water was removed.

The need for sufficient freezing time is reflected in Schemes Q and 12-24, which both required many more cycles and more days until tough gel formation than Scheme 24. The primary difference was Schemes Q and 12-24 had freezing cycle times of around 0.5 days instead of 1 day. However, schemes that had

longer cycling times than 1 day required many more days until gel formation. When dried, many of those gels collapsed to solid material when dried. While it is not clear why that occurs, it may be that these gels require more aggressive drying such as using supercritical methods (52) or freeze-drying to avoid a liquid state capable of collapsing pores through high surface tension (53). When much smaller samples were dried, the resulting solid was often white and appeared grindable. Any grindable foams produced were ground into powder of heterogeneous dimensions ranging from 10 to 1000 μm , as shown in Figure 1.

Characterization of PHBV:SF Foams

Results

Impact of SF on PHBV Foam Density and Cell Density

The SF powder was used as an additive in PHBV foaming at 1 (P99S1) and 5 wt% (P95S5) SF. Figures 13 and 14 show the resulting foams for neat PHBV and SF/PHBV, respectively, at AZ content from 0.5 to 4 phr. In general, with increasing blowing agent content, bulk density decreased and cell density increased. The differences between the foams are not drastic. As shown in Figure 15(a), the SF powder is less dense and is able to reduce the bulk density of unfoamed PHBV from 1.43 g/mL to 1.22 g/mL. This continues to reduce the density of 0.5 phr and 4 phr AZ foams. The bulk density of 1, 2, and 3 phr AZ foams were mostly unchanged though the cell densities at these AZ contents were lower for P99S1 than PHBV. Cell density only improved for 0.5 phr AZ.

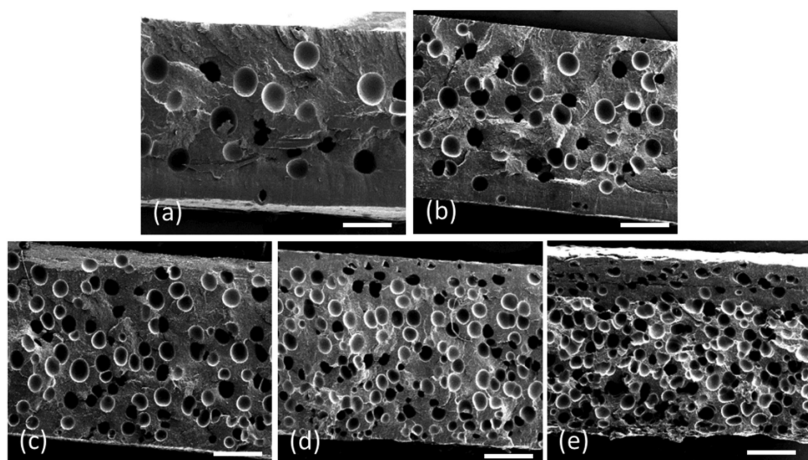


Figure 13. SEM images of PHBV foams blown with (a) 0.5, (b) 1, (c) 2, (d) 3, (e) 4 phr AZ at 80 rpm screw speed. Scale bars are 500 μm .

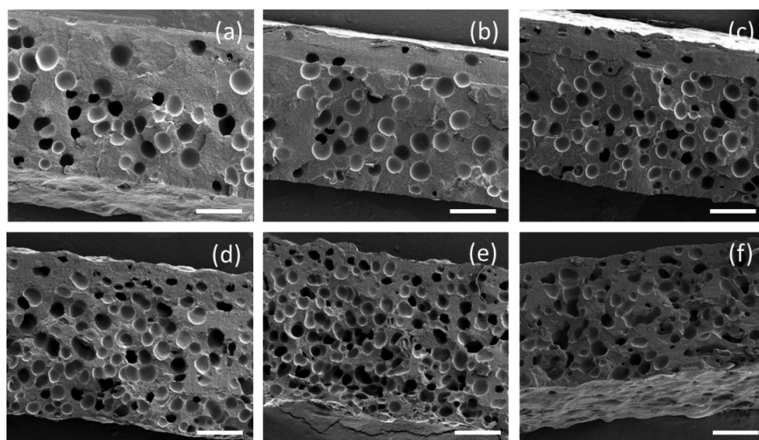


Figure 14. SEM images of PHBV foams with 1 wt% SF blown with (a) 0.5, (b) 1, (c) 2, (d) 3, (e) 4 phr AZ at 80 rpm screw speed, and (f) PHBV foam with 5 wt% SF blown with 4 phr AZ. Scale bars are 500 μm .

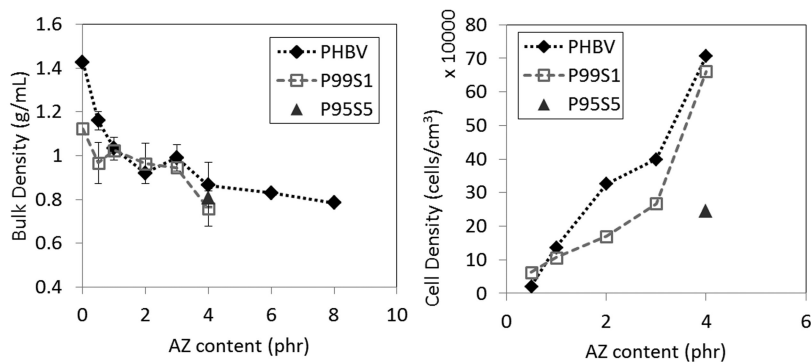


Figure 15. (a) Bulk density and (b) cell density of PHBV foams and PHBV/SF foams with a range of blowing agent contents.

During extrusion, the SF foams exhibited significant shrinkage during the cooling process after initial expansion upon exiting the extruder. From the SEM images in Figure 14(a)-(f), the upper and lower surfaces of the foam appear more rough due to shrinkage of the foams, especially compared to the surfaces of foams in Figure 13(a)-(e). Shrinkage occurs due to cooling of the gas and diffusion of the gas out faster than air can diffuse in (54). To evaluate the degree of shrinkage of foams during cooling, surface roughness of the foams was determined by drawing over the upper and lower surface lines in ImageJ to measure the actual rough surface length, l_R , and measuring the end-to-end distance of the upper and lower surface as a line, l_S . The roughness ratio, R , was determined as

$$R = \frac{l_R}{l_S}$$

Figure 16 shows the average roughness ratio of the top and bottom surfaces for the various AZ contents. P99S1 shows increasingly more shrinkage at contents above 0.5 phr AZ. In contrast, neat PHBV does not exhibit shrinkage until 4 phr AZ. Table V lists the calculated bulk density of foams pre-shrinkage depending on whether shrinkage is assumed to uniformly occur only in 1D (i.e., the width) or up to 3D (i.e., length, width, and height of the foam). With this adjustment, the bulk density of P99S1 foam with 4 phr AZ could be as low as 0.66 g/mL.

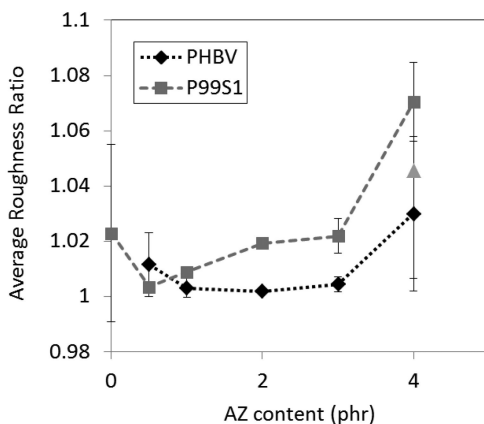


Figure 16. Average roughness ratio of PHBV/SF foams.

Table V. Adjusted foam bulk density based on shrinkage of P99S1 foams

<i>AZ content (phr)</i>	<i>Roughness ratio</i>	<i>Non-adjusted bulk density (g/mL)</i>	<i>1D adjusted bulk density (g/mL)</i>	<i>3D adjusted bulk density (g/mL)</i>
0	1.023	1.12	1.10	1.07
0.5	1.003	0.97	0.96	0.96
1	1.009	1.03	1.02	1.01
2	1.019	0.96	0.95	0.93
3	1.022	0.95	0.93	0.91
4	1.070	0.76	0.71	0.66

Discussion: Overall Impact of SF Content on PHBV/SF Foams

Because 1 wt% SF decreased bulk density of the PHBV matrix, and reduced the overall foam density achievable, it was possible that increasing the SF content may further improve on these areas as well as have a greater impact on cell density. However, the higher SF content of P95S5 foams did not improve bulk density beyond that of P99S1 because there was extremely low cell density in Figure 15(b). From the SEM images, significant cell coalescence can be observed in P99S5. To accentuate the cell coalescence, binary images of the foam structure from SEM were drawn using ImageJ software and are compared in Figure 17. The large, irregularly shaped features in Figure 17(c) suggest the coalescence of multiple neighboring cells, which reduces the observed cell density multifold. Additionally, the height of the foam clearly decreases with increasing SF content as shown by the diminished dimensions occupied by cells. This indicates that there was also significant gas loss and shrinkage. From Figure 14(f), the bottom surface of the foam can be observed and there are many holes where gas escaped. Though the roughness ratio was determined to be intermediate to PHBV and P99S1, the variability was very high due to differences in the top and bottom surface roughness, so that shrinkage is expected to be more significant than was calculated.

The increased content of SF appears to promote cell coalescence. If the SF is nucleating more cells, the sudden diffusion of gas to these lower pressure areas may result in cell coalescence if melt strength of PHBV is insufficient to withstand the expansion at the cell wall. Because more shrinkage also occurs in neat PHBV foams at 4 phr AZ, this is likely a major contribution. Another explanation could be that the presence of more SF particles on the cell walls may promote bursting of cell walls since the SF and PHBV are immiscible. If the cell wall is thinner than a particle embedded in the cell wall, the interfacial energy between the particle and the liquid will determine whether the wall will drain more quickly or slowly (54). In the case of SF and PHBV, which are not miscible, the SF particle will likely cause faster drainage of the wall leading to coalescence.

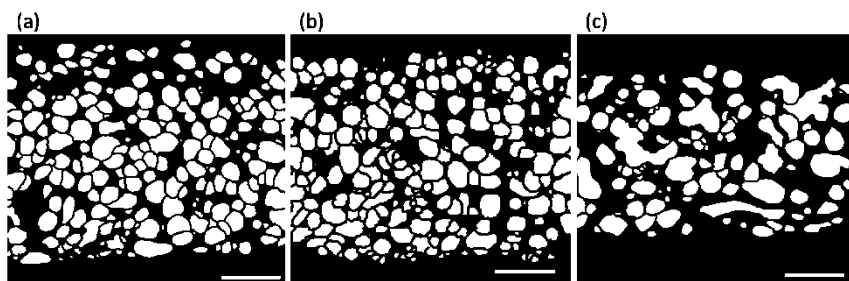


Figure 17. Binary images traced from SEM micrographs comparing the cell coalescence in (a) PHBV, (b) P99S1, and (c) P95S5 foams with 4 phr AZ. Scale bar is 500 μm .

Conclusions

It was determined that PHBV and SF were immiscible across the range of compositions studied. However, the two phases still had mutual influence on thermal properties and morphology. The hydrophobic nature of PHBV promotes crystallization of the hydrophobic SF regions to form β -sheets that result in high crystallinity and higher thermal stability of the SF phase. SF also acts as a crystal nucleating agent for PHBV, but is excluded to the interspherulitic regions during PHBV crystal growth. Below 20 wt% SF, crystallinity decreased and degradation temperature more rapidly decreased suggesting more interaction between the phases in this range.

Following melting and fast cooling in the DSC, PHBV melting temperature and crystallinity were generally reduced below that of neat PHBV films processed in the same way. The new PHBV crystals are likely nucleated in regions of higher SF content hindering the already shortened crystallization process. At 1 wt% SF, melting temperature and crystallinity are higher because of less SF to hinder growth. Unfortunately, PHBV degradation temperatures were monotonically reduced with increasing SF content. The addition of water bound to SF can promote hydrolysis and more mobile chain ends at the SF/PHBV interface can lead to more chain backbiting as part of thermal degradation. Subsequently, low contents of SF should be used for foaming to minimize potential for hydrothermal degradation while utilizing the nucleating properties.

To produce SF powder for foam extrusion, it was found that 3 cycles of 1-day freeze-thaw cycles were able to reproducibly yield SF aerogels from tough hydrogels after drying in a vacuum oven. Shorter cycles required many more periods and were less reproducible. Hydrogels formed with longer cycles required significantly more days to yield a tough hydrogel, and were more difficult to dry completely or collapsed to a solid. The freezing step was important in forming the porous structure and driving the SF to self-associate and form a tough gel.

Though SF powder was found to be lighter than PHBV and thus reduced the bulk density of unfoamed PHBV, it only improved foam density for 0.5 and 4 phr AZ at 1 wt% SF. For the intermediate AZ contents, cell density was more significantly below that of neat PHBV so bulk density was not enhanced. When

5 wt% SF was added with 4 phr AZ, there was substantial cell coalescence so cell density was drastically reduced. Using the roughness ratio, it was shown there there is greater foam shrinkage in foams with SF. SF may be promoting gas diffusion out of the matrix and may destabilize cell walls due to immiscibility. The poor PHBV melt strength must be improved before SF can have a significant impact.

Acknowledgments

This material is based upon work supported by the National Science Foundation Graduate Research Fellowship under Grant No. DGE-1147470. Any opinion, findings, and conclusions or recommendations expressed in this material are those of the authors and do not necessarily reflect the views of the National Science Foundation. The authors would also like to thank Dr. Carmen Preda for support in producing silk fibroin and Dr. Yilin Chung for help with GPC measurements. A portion of this work was performed at the Stanford Nanocharacterization Laboratory (SNL) part of the Stanford Nano Shared Facilities and the NIH P41 resource center on Tissue Engineering (EB002520).

References

1. Maier, C.; Calafut, T. *Polypropylene: The Definitive User's Guide and Databook*; Plastics Design Library: Norwich, NY, 1999.
2. Doi, Y. *Microbial Polyesters*; VCH Publishers: New York, 1990.
3. Srubary, W. V.; Wright, Z. C.; Tsui, A.; Michel, A. T.; Billington, S. L.; Frank, C. W. *Polym. Degrad. Stab.* **2012**, *97*, 1922–1929.
4. Liao, Q.; Tsui, A.; Billington, S. L.; Frank, C. W. *Polym. Eng. Sci.* **2012**, *52*, 1495–1508.
5. Javadi, A.; Srithep, T.; Pilla, S.; Clemons, C.; Turng, L. S.; Gong, S. *Soc. Plast. Eng., Plast. Res. Online* **2011**, 1–4.
6. Verhoogt, H.; Ramsay, B. A.; Favis, B. D. *Polymer* **1994**, *35*, 5155–5169.
7. Richards, E.; Rizvi, R.; Chow, A.; Naguib, H. *J. Polym. Environ.* **2008**, *16*, 258–266.
8. Buchanan, C. M.; Gedon, S. C.; White, A. W.; Wood, M. D. *Macromolecules* **1992**, *25*, 7371–7381.
9. Kubo, S.; Kadla, J. F. *Biomacromolecules* **2003**, *4*, 561–567.
10. Thirtha, V.; Lehman, R.; Nosker, T. *Polymer* **2006**, *47*, 5392–5401.
11. Thirtha, V.; Lehman, R.; Nosker, T. *Polym. Eng. Sci.* **2005**, *45*, 1187–1193.
12. Ash, B. J.; Siegel, R. W.; Schadler, L. S. *J. Polym. Sci., Part B.: Polym. Physics* **2004**, *42*, 4371–4383.
13. Fu, C.; Shao, Z.; Fritz, V. *Chem. Commun. (Cambridge, U.K.)* **2009**, 6515–6529.
14. Sun, M.; Zhou, P.; Pan, L.-F.; Liu, S.; Yang, H.-X. *J. Mater. Sci.: Mater. Med.* **2009**, *20*, 1743–1751.
15. Vepari, C.; Kaplan, D. L. *Prog. Polym. Sci.* **2007**, *32*, 991–1007.
16. Numata, K.; Cebe, P.; Kaplan, D. L. *Biomaterials* **2010**, *31*, 2926–2933.

17. Breslauer, D. N.; Kaplan, D. L. In *Polymer Science: A Comprehensive Review*; Matyjaszewski, K., Möller, M., Eds.; Elsevier B.V.: Waltham, MA, 2012; Vol. 9, pp 57–69.
18. He, S. J.; Valluzzi, R.; Gido, S. P. *Int. J. Biol. Macromol.* **1999**, *24*, 187–195.
19. Sashina, E. S.; Novoselov, N. P.; Heinemann, K. *Russ. J. Appl. Chem.* **2005**, *78*, 153–158.
20. Yang, H. *J. Biomed. Sci. Eng.* **2010**, *3*, 1146–1155.
21. Sudesh, K.; Hideki, A. *Practical Guide to Microbial Polyhydroxyalkanoates*; Smithers Rapra Technology: Shawbury, U.K., 2010; pp 25–50.
22. Peng, S. *Eur. Polym. J.* **2003**, *39*, 1475–1480.
23. Kang, D. J.; Xu, D.; Zhang, Z. X.; Pal, K.; Bang, D. S.; Kim, J. K. *Macromol. Mater. Eng.* **2009**, *294*, 620–624.
24. Kim, U. -J.; Park, J.; Li, C.; Jin, H. -J.; Valluzzi, R.; Kaplan, D. L. *Biomacromolecules* **2004**, *5*, 786–792.
25. Nazarov, R.; Jin, H. -J.; Kaplan, D. L. *Biomacromolecules* **2004**, *5*, 718–726.
26. Motta, A.; Fambri, L.; Migliaresi, C. *Macromol. Chem. Phys.* **2002**, *203*, 1658–1665.
27. Nakamura, S.; Magoshi, J.; Magoshi, Y. In *Silk Polymers: Materials Science and Biotechnology*; Kaplan, D. L., Adams, W. W., Farmer, B., Viney, C., Eds.; ACS Symposium Series 544; American Chemical Society: Washington, DC, 1993; pp 211–221.
28. Barham, P. J.; Keller, A.; Otun, E. *J. Mater. Sci.* **1984**, *19*, 2781–2794.
29. Shanks, R. A.; Amarasinghe, G. In *Polymer Characterization Techniques and the Application to Blends*; Simon, G. P., Ed.; Oxford University Press: New York, 2003; pp 22–67.
30. Renard, E.; Walls, M.; Guérin, P.; Langlois, V. *Polym. Degrad. Stab.* **2004**, *85*, 779–787.
31. Liu, Q.-S.; Zhu, M.-F.; Wu, W.-H.; Qin, Z.-Y. *Polym. Degrad. Stab.* **2009**, *94*, 18–24.
32. Cheng, M.-L.; Sun, Y.-M.; Chen, H.; Jean, Y. C. *Polymer* **2009**, *50*, 1957–1964.
33. Reis, K.; Pereira, J.; Smith, A.; Carvalho, C.; Weller, N.; Yakimets, I. *J. Food Eng.* **2008**, *89*, 361–369.
34. Tian, G.; Wu, Q.; Sun, S.; Noda, I.; Chen, G.-Q. *Appl. Spectrosc.* **2001**, *55*, 888–893.
35. Hu, X.; Kaplan, D. L.; Cebe, P. *Macromolecules* **2008**, *41*, 3939–3948.
36. Hu, X.; Kaplan, D. L.; Cebe, P. *Macromolecules* **2006**, *39*, 6161–6170.
37. Gil, E. S.; Frankowski, D. J.; Bowman, M. K.; Gozen, A. O.; Hudson, S. M.; Spontak, R. J. *Biomacromolecules* **2006**, *7*, 728–735.
38. Buzarovska, A.; Grozdanov, A. *J. Mater. Sci.* **2009**, *44*, 1844–1850.
39. Glišović, A.; Salditt, T. *Appl. Phys. A: Mater. Sci. Process.* **2007**, *87*, 63–69.
40. Magoshi, J.; Nakamura, S. *J. Appl. Polym. Sci.* **1975**, *19*, 1013–1015.
41. Tanaka, H.; Nishi, T. *Phys. Rev. Lett.* **1985**, *55*, 1102–1105.
42. Di Lorenzo, M. L. *Prog. Polym. Sci.* **2003**, *28*, 663–689.
43. Genovese, A.; Shanks, R. A. *J. Appl. Polym. Sci.* **2003**, *90*, 175–185.
44. Nam, J.; Park, Y. H. *J. Appl. Polym. Sci.* **2001**, *81*, 3008–3021.

45. Pierre, A. C. In *Aerogels Handbook*; Aegerter, M. A., Leventis, N., Koebel, M. M., Eds.; Springer: New York, 2011; pp 3–18.
46. Nagarkar, S.; Nicolai, T.; Chassenieux, C.; Lele, A. *Phys. Chem. Chem. Phys.* **2010**, *12*, 3834–3844.
47. Jin, H.-J.; Kaplan, D. L. *Nature* **2003**, *424*, 1057–1061.
48. Matsumoto, A.; Chen, J.; Collette, A. L.; Kim, U. -J.; Altman, G. H.; Cebe, P.; Kaplan, D. L. *J. Phys. Chem. B* **2006**, *110*, 21630–21638.
49. Stauffer, S. R.; Peppas, N. A. *Polymer* **1992**, *33*, 3932–3936.
50. Peppas, N. A.; Stauffer, S. R. *J. Controlled Release* **1991**, *16*, 305–310.
51. Li, M.; Lu, S.; Wu, Z.; Yan, H.; Mo, J.; Wang, L. *J. Appl. Polym. Sci.* **2001**, *79*, 2185–2191.
52. Kistler, S. S. *Nature* **1931**, *127*, 741–741.
53. Fricke, J.; Tillotson, T. *Thin Solid Films* **1997**, *297*, 212–223.
54. Zhang, X. D.; Neff, R. A.; Macosko, C. W. In *Polymer Foams: Mechanisms and Materials*; Lee, S. T., Ramesh, N. S., Eds.; CRC Press: Boca Raton, FL, 2004.